



MASTER IN ASTROPHYSICS  
AND SPACE SCIENCE

Erasmus Mundus Master  
in Astrophysics and Space Science

Master Thesis

# High-Contrast Imaging of Exoplanetary Systems with Very Large Telescopes

**Supervisors:**

Dr. Gael Chauvin  
Lab. Lagrange, Observatoire Côte d'Azur

Dr. Valentina D'Orazi  
Dipartimento di Fisica, Università di Roma Tor Vergata

**Author:**

Macarena C. Vega Pallauta

Academic Year 2023/2024



This Master thesis is submitted in partial fulfillment of the requirements for the degree «Master Physique fondamentale et applications, parcours MASS» as part of a multiple degree awarded in the framework of the Erasmus Mundus Joint Master in Astrophysics and Space Science – MASS jointly delivered by a Consortium of four Universities: Tor Vergata University of Rome, University of Belgrade, University of Bremen, and Université Cote d’Azur, regulated by the MASS Consortium Agreement and funded by the EU under the call ERASMUS-EDU-2021-PEX-EMJM-MOB.

# Contents

|  |           |
|--|-----------|
| Abstract . . . . .   | 1         |
| <b>1 Introduction</b>  | <b>2</b>  |
| 1.1 Circumstellar Disks . . . . .                                  | 3         |
| 1.1.1 Protoplanetary Disks . . . . .                               | 3         |
| 1.1.2 Debris Disks . . . . .                                       | 4         |
| 1.2 Outline of the thesis . . . . .                                | 5         |
| <b>2 High-Contrast Imaging</b>                                     | <b>6</b>  |
| 2.1 Challenges . . . . .   | 7         |
| 2.2 Obs. Techniques . . . . .                                      | 9         |
| 2.2.1 Adaptive Optics . . . . .                                    | 10        |
| 2.2.2 Coronagraphy . . . . .                                       | 11        |
| 2.2.3 Angular Differential Imaging . . . . .                       | 12        |
| 2.2.4 Reference Differential Imaging . . . . .                     | 14        |
| 2.2.5 Spectral Differential Imaging . . . . .                      | 14        |
| 2.3 Principal Component Analysis . . . . .                         | 15        |
| 2.4 SHARK-NIR . . . . .  | 17        |
| 2.5 SPHERE . . . . .   | 23        |
| <b>3 SHARK-NIR observations of the protoplanetary disk MWC 758</b> | <b>26</b> |
| 3.1 The protoplanetary disk MWC 758 . . . . .                      | 27        |
| 3.2 Observations and data reduction . . . . .                      | 28        |
| 3.3 Image processing . . . . .                                     | 28        |

|          |  |           |
|----------|--|-----------|
| 3.3.1    | Frame filtering . . . . .                              | 28        |
| 3.3.2    | Post-processing . . . . .                              | 29        |
| 3.4      | Results and Analysis . . . . .                         | 31        |
| 3.4.1    | Detection limits . . . . .                             | 32        |
| 3.5      | Discussion . . . . .                                   | 33        |
| <b>4</b> | <b>SPHERE observations of the debris disk HD 95086</b> | <b>38</b> |
| 4.1      | The young system HD 95086 . . . . .                    | 40        |
| 4.2      | Observations . . . . .                                 | 41        |
| 4.3      | Image Processing . . . . .                             | 43        |
| 4.3.1    | Frame-filtering . . . . .                              | 43        |
| 4.3.2    | Post-processing . . . . .                              | 44        |
| 4.4      | Forward Modeling . . . . .                             | 46        |
| 4.4.1    | Astrometry and photometry . . . . .                    | 47        |
| 4.4.2    | Spectral analysis . . . . .                            | 50        |
| 4.5      | Detection Limits . . . . .                             | 51        |
| 4.5.1    | Contrast Curves . . . . .                              | 51        |
| 4.5.2    | Probability Maps . . . . .                             | 52        |
| 4.6      | Discussion . . . . .                                   | 54        |
| <b>5</b> | <b>Conclusions</b>                                     | <b>56</b> |
| <b>A</b> | <b>Observational conditions for HD 95086</b>           | <b>64</b> |
| <b>B</b> | <b>Frame Correlation Analysis for Image Filtering</b>  | <b>66</b> |
| <b>C</b> | <b>Poster Presentation: Sagan Summer Workshop</b>      | <b>68</b> |



---

## Abstract

This thesis presents the data reduction and analysis of high-contrast imaging observations of two astronomical systems: the protoplanetary disk MWC 758 and the planetary system HD 95086. Observations of MWC 758 were conducted using the SHARK-NIR instrument with a Gaussian Lyot coronagraph, employing Angular Differential Imaging (ADI) and Reference Differential Imaging (RDI) techniques. The images were processed using an iterative Principal Component Analysis (PCA) approach. These methods resolved the disk's two-spiral-arm structure in detail but did not confirm any companion candidates.

For HD 95086, we used SPHERE/IRDIS and SPHERE/IFS near-infrared observations, performed using the "star-hopping" technique, applying ADI and RDI+ADI techniques. The images were reduced using PCA following a similar approach as for the MWC 758 dataset. Our analysis focused on the known planet b and the search for additional companions. While no new candidates were found, we placed important constraints on the presence of additional giant planets.

Comparative analyses with archival data showed no significant morphological evolution in MWC 758's disk features, while for HD 95086, we obtained astrometric and photometric measurements of planet b. This research highlights the capabilities of state-of-the-art instruments in high-contrast imaging of protoplanetary disks and exoplanetary systems, contributing to the ongoing refinement of exoplanet detection and characterization techniques.

# Chapter 1

## Introduction

The discovery and study of exoplanets have revealed diverse architectures and different types of planets beyond our Solar System. High-contrast imaging, in particular, allows us to directly observe gas giant exoplanets within circumstellar disks. These disks undergo significant changes throughout their lifetime, transitioning from gas-rich protoplanetary disks to gas-poor debris disks. Protoplanetary disks are active sites of planet formation. In contrast, debris disks, typically observed around young stars, represent the by-product of planet formation processes. By studying systems at these different evolutionary stages, we can gain insights into the complex mechanisms of planet formation and early system evolution.

This thesis focuses on the observation and analysis of two systems representing different stages in this evolutionary sequence. MWC 758, a very young Herbig star (3.5 Myr, 160 pc, spectral type A8Ve) hosting a protoplanetary disk, where planet formation could be ongoing, and HD 95086 (13.3 Myr, 86 pc, spectral type A8), surrounded by a debris disk. These two systems are thought to host more planets than have been discovered to date, to explain their observed morphologies.

This work aims to characterize these systems using high-contrast imaging observations. We seek to search for new, previously undetected planetary companions or,

in the case of non-detections, to provide constraints on their possible locations and masses based on our observations and analysis.

## 1.1 Circumstellar Disks

### 1.1.1 Protoplanetary Disks

Protoplanetary disks are a common feature around young stars ( $\leq 10$  Myr), as evidenced by infrared and millimeter excess emission in the spectral energy distributions of most pre-main-sequence stars (Chen et al., 2016). These disks typically have a lifetime of about 10 million years, during which most of the disk gas is accreted onto the central star. This timescale sets a crucial constraint on planet formation, with current results suggesting that planets might take 5-10 million years to form (Pfalzner et al., 2022). As planets form and evolve within these disks, they perturb the surrounding dust, creating asymmetries, spiral arms, and visible gaps in the disk structure. These features serve as tracers of exoplanet formation, potentially revealing the existence, location, and mass of yet-undetected forming planets (See Figure 1.1).

Several mechanisms have been proposed to explain how giant planets form within protoplanetary disks. The core accretion model (Pollack et al., 1996) suggests that rocky cores form first through the gradual accumulation of dust and planetesimals, potentially followed by gas accretion. Alternatively, the disk instability model (Boss, 1997) proposes that portions of a massive disk can collapse directly into gas giant planets. These formation pathways can lead to different initial conditions for young planets, often categorized as “cold start” or “warm/hot start” models, which have implications for the planets’ subsequent evolution and observable properties (Spiegel & Burrows, 2012).

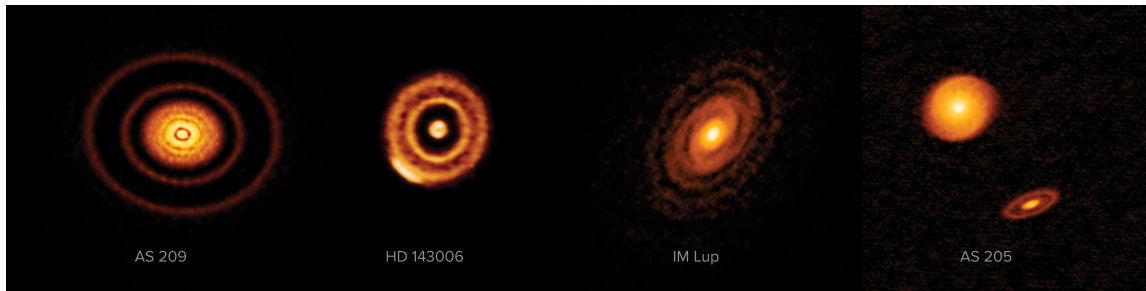


Figure 1.1: Four of the twenty disks included in ALMA’s highest resolution survey of nearby protoplanetary disks, known as the Disk Substructures at High Angular Resolution Project (DSHARP). Credit: ALMA (ESO/NAOJ/NRAO) [Andrews et al. \(2018\)](#); NRAO/AUI/NSF, S. Dagnello

### 1.1.2 Debris Disks

Debris disks represent a later stage in the evolution of circumstellar disks, typically found around main sequence stars older than about 10 million years. These disks emerge after most of the material in the protoplanetary disk has been dissipated or incorporated into larger bodies. Primarily composed of dust with little to no gas, debris disks are optically thin and often exhibit complex structures that may resemble to our Solar System’s asteroid and Kuiper belts ([Wyatt, 2008](#)). The dust in these disks is continuously replenished through collisions between larger bodies, as the original protoplanetary dust has been lost. Debris disks are often detected through their infrared or millimeter excess emission, resulting from dust heated by stellar radiation. They can be imaged in thermal emission from the mid-infrared to the millimeter, or in scattered light in the optical or in the near-infrared ([Pearce, 2024](#)). They typically feature warm inner and cold outer components, with solids ranging from sub-micron dust to kilometer-sized planetesimals ([Hughes et al., 2018](#)). Found around a significant fraction of nearby stars, debris disks provide unique opportunities to study planet-disk interactions and potentially image planets within them (See Figure 1.2).

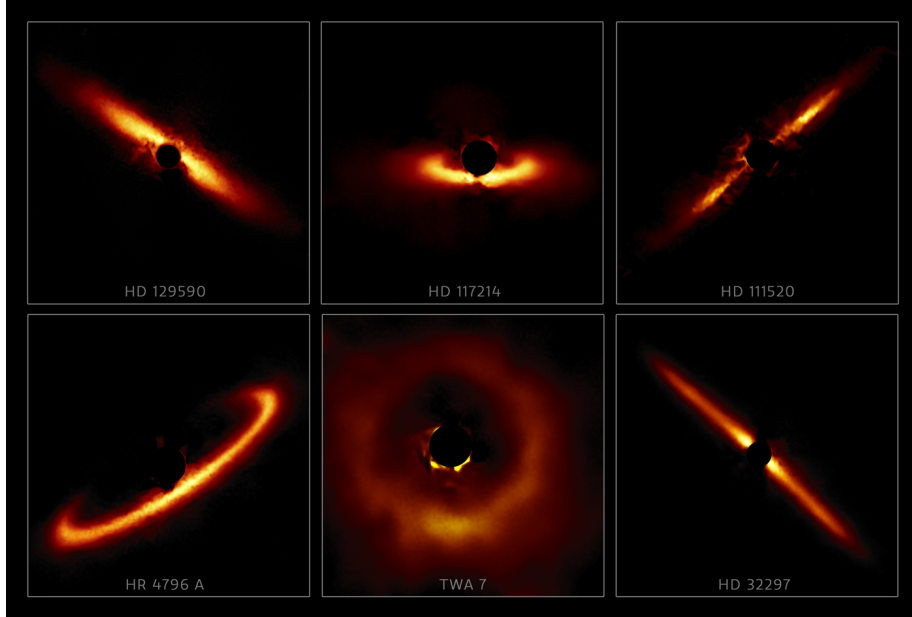


Figure 1.2: Debris disks obtained from the Gemini Planet Imager Exoplanet Survey’s Polarimetric Imaging Campaign (Esposito et al., 2020). Credit: NOIRLab

## 1.2 Outline of the thesis

This thesis is organized into three main chapters, each one addressing an aspect of the characterization of young exoplanetary systems embedded in circumstellar disks. In Chapter 2, we present a comprehensive description of the high-contrast imaging detection method, providing an overview of the techniques employed to overcome its inherent challenges. This chapter also introduces the instruments used to collect the data used in this research. In Chapter 3, we investigate the morphology of the protoplanetary disk MWC 758 using the SHARK-NIR instrument, and present detection capabilities of the instrument in terms of extended structures resolution. Chapter 4 focuses on the characterization of the planet hosted by the young debris disk HD 95086, along with an analysis of the detection limits achievable with SPHERE. Finally, Chapter 5 summarizes the key findings and insights obtained from this research, highlighting their significance in the context of exoplanetary studies.

# Chapter 2

## High-Contrast Imaging

High-contrast imaging (HCI), together with nulling interferometry, are the only direct methods used in exoplanetary research to capture images of planets outside our Solar System ("exoplanets"). Unlike other techniques that rely on indirect signals, HCI directly observes the faint light emitted or reflected by exoplanets, providing a direct visual approach to studying their orbital motion, characteristics and atmospheres.

As of March 9, 2024, there are over 5,756 confirmed exoplanets, of which 82 have been discovered through imaging techniques <sup>1</sup>. While this represents a small fraction of the total, HCI plays a crucial role in exoplanet research due to its particular sensitivity for observing young, self-luminous giant exoplanets that orbit their host stars at significant distances (Figure 2.1). These systems are of particular interest as they offer insights into the early stages of planetary formation and the dynamics of wide-orbit companions. This constrains the pool of observations to young stars (hundreds of Myr) located at distances of few hundred parsecs, for which the planets are still warm (Chauvin, 2018).

---

<sup>1</sup>[https://exoplanetarchive.ipac.caltech.edu/docs/counts\\_detail.html](https://exoplanetarchive.ipac.caltech.edu/docs/counts_detail.html)

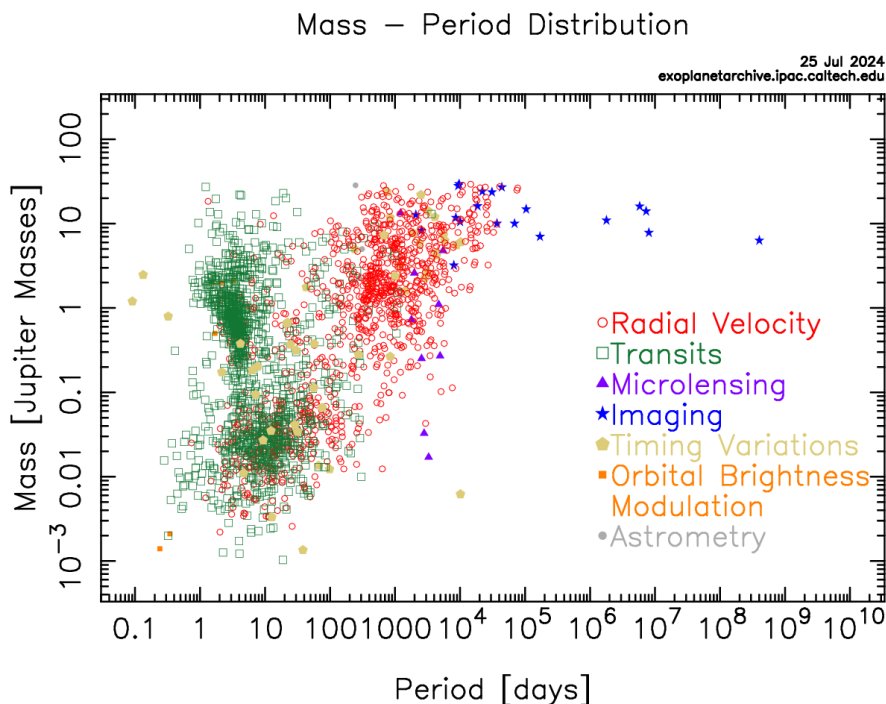


Figure 2.1: Current status of the 5,756 planets being detected by different methods (from <https://exoplanetarchive.ipac.caltech.edu/exoplanetplots/>)

## 2.1 Challenges

The primary challenge lies in the intense brightness of host stars, which outshines the planets’ flux. Contrasts when implementing Adaptive Optics and coronagraphs (See section 2.2) typically reach  $10^{-3} - 10^{-4}$  (Figure 2.2), while exoplanets detected so far have brightness contrasts of  $10^{-5} - 10^{-6}$  (or brighter) compared to their host stars. To put this in perspective, detecting a Jupiter-like planet in reflected light requires a contrast of  $10^{-9}$ , while an Earth-like planet would need a contrast of  $10^{-10}$  (Fujii et al. (2018), Figure 2.3).

In the case of thermal emission, the age of the planetary system plays a crucial role in our ability to detect planets directly. Young planets are significantly brighter in thermal emission due to residual heat from their formation. As planets cool over time, their thermal emission decreases, making them progressively harder to detect.

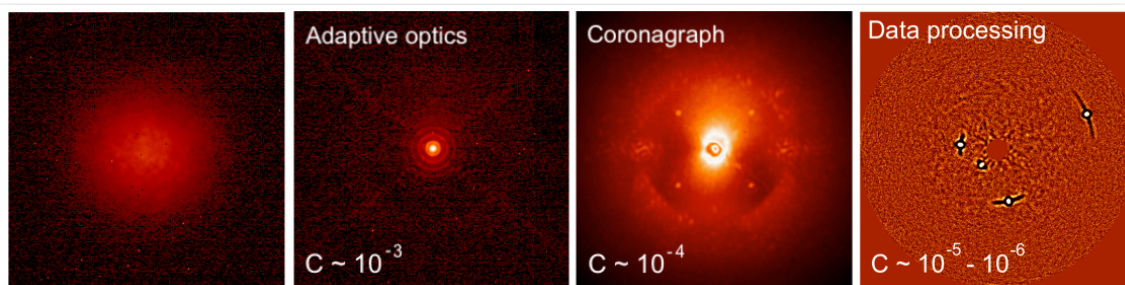


Figure 2.2: High-contrast imaging techniques. From *left to right*: (1) A typical ground-based stellar image without adaptive optics; (2) The same image with adaptive optics, enhancing angular resolution; (3) Further improvement with a coronagraph, suppressing the star’s halo; (4) Final result after post-processing, showing the HR 8799 system. Credits: SPHERE commissioning team and Faustine Cantalloube.

From the different sources that can affect the contrast, the main contributor is generally the speckle noise, in particular the noise coming from the quasi-static speckles arising from imperfections in the telescope and optical system, mechanical movements, and temperature changes. The temporal evolution of these speckles ranges from the order of seconds to several minutes (Martinez et al., 2012). To reach the contrasts required for disk imaging and exoplanet detection, the starlight and its residuals, together with speckles generated by the instrument and the atmosphere must be removed from the images. To overcome this, specialized tools like coronagraphs, adaptive optics (AO), and specific dataprocessing techniques are employed to enhance the contrast in the images. Coronagraphs block the starlight making the brightest planets visible, while adaptive optics compensate for atmospheric distortions, allowing for clearer images. However, these techniques alone are usually insufficient to detect faint signals. Advanced post-processing methods use the diversity between stellar and circumstellar signals to construct and subtract the residual stellar light and reveal planets or disks.



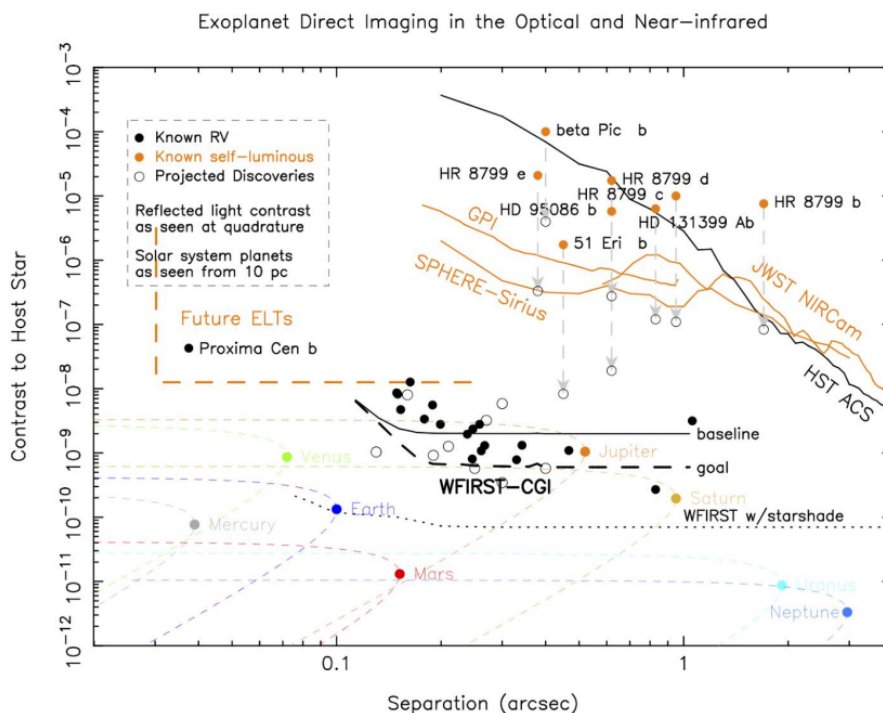


Figure 2.3: Performance of existing and future high-contrast imaging ground-based (*yellow*) and space-based (*black*) instruments. From Fujii et al. (2018)

## 2.2 Observing techniques

Exoplanets are imaged using various techniques to enhance angular resolution and contrast. To mention some of them, larger apertures improve signal-to-noise ratio and resolution; adaptive optics minimize atmospheric turbulence, while space-based imaging avoids these effects entirely; coronagraphic masks suppress stellar light, and post-processing corrects residual aberrations; interferometers enhance angular resolution, and in the case of nulling interferometry, the stellar light is eliminated by destructive interference.

The most important techniques for the scope of this work are adaptive optics, coronagraphy, differential imaging and speckle subtraction through Principal Component Analysis, described in the following sections.

### 2.2.1 Adaptive Optics

Imaging exoplanets is extremely challenging even for the biggest telescopes currently in operation. This is because the resolution of all ground-based telescopes is limited by the atmospheric conditions of the place where they are installed. Not only that but also the structure of the telescope itself produces diffraction patterns that distort the images. To mitigate this effect and approach the diffraction limit of the telescope ( $\theta \approx \lambda/D$ ), adaptive optics and active optics techniques are implemented.

Adaptive optics aim to compensate for atmospheric phase fluctuations across the telescope pupil. The process involves three main components: the wavefront sensor, the deformable mirror, and the control system (Figure 2.4).

- **Wavefront Sensing:** As light from a target star propagates through the turbulent atmosphere, it undergoes phase fluctuations. Wavefront sensing involves the continuous measurement of these atmospheric phase fluctuations by analyzing the wavefront of a nearby bright reference star. This measurement captures the distortions caused by atmospheric turbulence.
- **Wavefront Control with a Deformable Mirror:** An equal but opposite wavefront correction is then imposed using wavefront control techniques. A deformable mirror, equipped with actuators distributed across behind its surface, is used for this purpose. These actuators adjust the shape of the mirror in almost real time to counteract the measured distortions, effectively flattening the incoming wavefront.
- **Control System:** The control system coordinates the measurements from the wavefront sensor with the adjustments made by the deformable mirror. It processes the data from the wavefront sensor, calculates the necessary corrections, and sends commands to the actuators on the deformable mirror. This system operates at high speed ( $\sim$  KHz), continuously updating the mirror's shape to keep up with the rapidly changing atmospheric conditions.

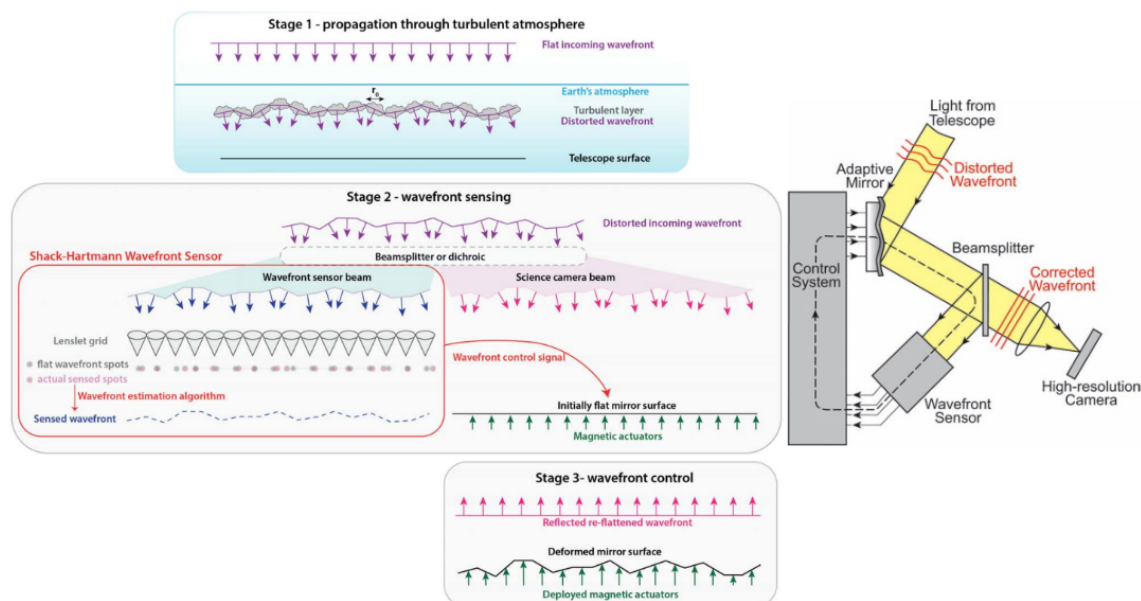


Figure 2.4: Illustration of atmospheric correction using an Adaptive Optics system. Merged from Follette (2023) and Tokunaga & Jedicke (2007).

High-contrast imaging with adaptive optics has significantly contributed to the field of exoplanet detection by enabling the investigation of separations exceeding 10 au and the detection of masses as low as  $1 M_J$  (Bowler, 2016).

## 2.2.2 Coronagraphy

Telescopes equipped with adaptive optics produce a point-spread function (PSF) with a bright diffraction-limited core and several Airy rings on a wide scattered light halo. This setup, although improved over atmospheric seeing, still faces limitations from the stellar halo and bright Airy rings. To further enhance contrast, coronagraphs are employed to suppress a significant part of the stellar halo. These instruments use masks in the telescope focal plane to block the central stellar light, allowing for deeper imaging of planetary systems. However, the coronagraph also creates diffraction rings around the star that need to be suppressed by a Lyot Stop (Figure

2.5).

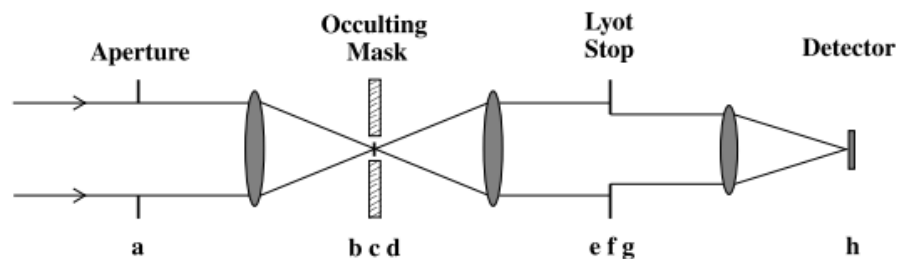


Figure 2.5: Schematic of a Lyot Stop coronagraph (Sivaramakrishnan et al., 2001)

The integration of coronagraphs with AO systems manages to suppress a significant part of the starlight and reduce bright diffraction rings and halos. However, given the extreme contrast ratios between stars and their circumstellar environment (Section 2.1), more stellar light must be suppressed. In the following sections, we will explore two key approaches: differential imaging techniques and principal component analysis, powerful methods for constructing and subtracting stellar light.

### 2.2.3 Angular Differential Imaging

Angular differential imaging (ADI) is a technique used to enhance the visibility of faint objects near bright sources, such as stars or exoplanets, within a telescope's field of view. This method is particularly effective in reducing quasi-static speckle noise.

ADI involves acquiring a sequence of images using an altitude/azimuth telescope with the instrument's field derotator turned off. This setup allows the telescope and instrument optics to remain fixed in their orientation while the celestial field of view rotates relative to the instrument as the Earth rotates. Each image in the sequence captures the scene at a slightly different rotation angle, effectively sampling different orientations of the sky relative to the instrument. During data processing, a reference PSF is constructed from the median combination of the image sequence.

Each individual image in the sequence is then corrected by subtracting this reference PSF, which effectively removes the quasi-static speckle patterns and leaves behind the residual light from any faint companions or background sources.

After subtraction, the residual images are “derotated” to align their fields of view based on their original sky orientations. This alignment ensures that all images are in the same coordinate system before they are combined or averaged together. The final step involves combining these derotated images, typically using a median combination technique once again (Marois et al., 2006). This process enhances the signal-to-noise ratio by averaging out random noise while preserving the signal from faint off-axis structures, thereby improving the clarity and contrast of the final image.

The classical ADI process is illustrated in image 2.6.

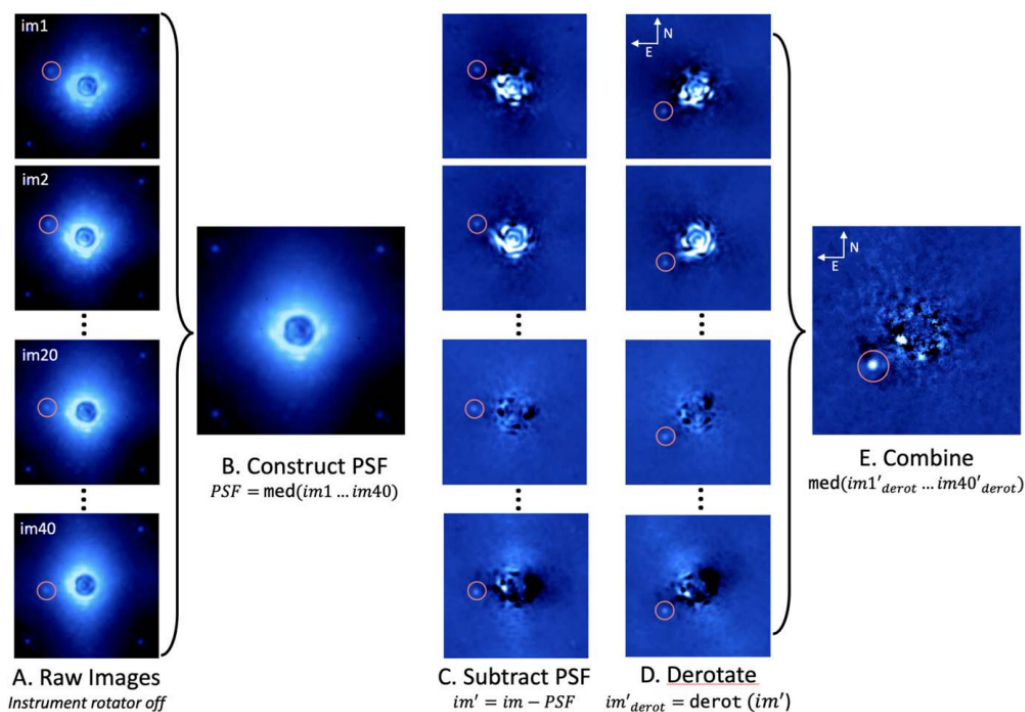


Figure 2.6: Schematic of the Angular Differential Imaging technique (Follette, 2023).

## 2.2.4 Reference Differential Imaging

When the target exhibits extended features such as disks, the classical ADI technique may not be optimal. This is because ADI typically involves median combining a sequence of images and subtracting a reference PSF, which can inadvertently remove the extended features along with the intended noise. Instead, the Reference Differential Imaging (RDI) technique offers a more suitable approach. In RDI, a reference PSF library is created using images of other stars taken at the same wavelength and in the same observing mode as the science target, typically with the same instrument and coronagraph settings. These reference stars are selected based on their proximity in the sky (often observed before or after the science target), similar apparent brightness at the wavelength of the wavefront sensor, and comparable color to ensure consistent performance of the adaptive optics system. The reference PSF allows for the subtraction of starlight from the target image, preserving extended features. The subtracted images are then rotated to a common on-sky orientation before being combined, following the same principle as in ADI. This process is illustrated in figure 2.7.

## 2.2.5 Spectral Differential Imaging

Spectral Differential Imaging (SDI) exploits the spectral differences between the central star and potential companions. An Integral Field Spectrograph (IFS) simultaneously obtains spectra for each spatial element in its field of view, producing a four-dimensional data cube with two spatial dimensions, one temporal dimension, and one spectral dimension  $(\lambda, n, x, y)$  (Sparks & Ford, 2002). This method involves comparing images at different wavelengths, typically chosen to coincide with and outside of absorption features in the spectrum of potential companions. For example, with SPHERE/IFS, one might compare images at wavelengths inside and outside methane absorption bands characteristic of cool, giant exoplanets. The images are scaled to account for the wavelength-dependent size of the PSF and then

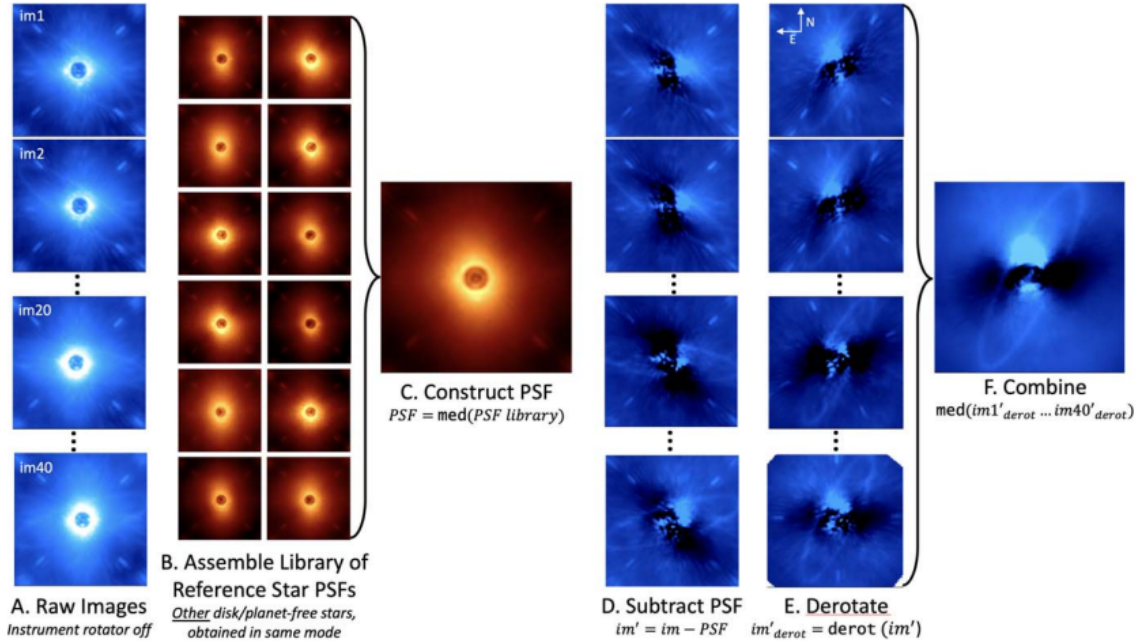


Figure 2.7: Schematic of the Reference Differential Imaging technique (Follette, 2023).

subtracted from each other. The subtracted images are then combined. This process is illustrated in figure 2.8. SDI with IFS data is particularly effective for detecting cool, methane-rich objects like T-type brown dwarfs or giant exoplanets, which have strong absorption features not present in hotter stellar spectra. However, it's important to note that SDI can lead to self-subtraction of companion signals, especially for companions at small angular separations. At small angular separations, the displacements of a companion caused by scaling images according to wavelength are smaller, which means more of the companion's signal may be present in the PSF model used for subtraction. This can lead to self-subtraction of the companion signal.

## 2.3 Principal Component Analysis

Principal Component Analysis (PCA) is a statistical technique used to reduce the dimensionality of large datasets while preserving as much of the original information



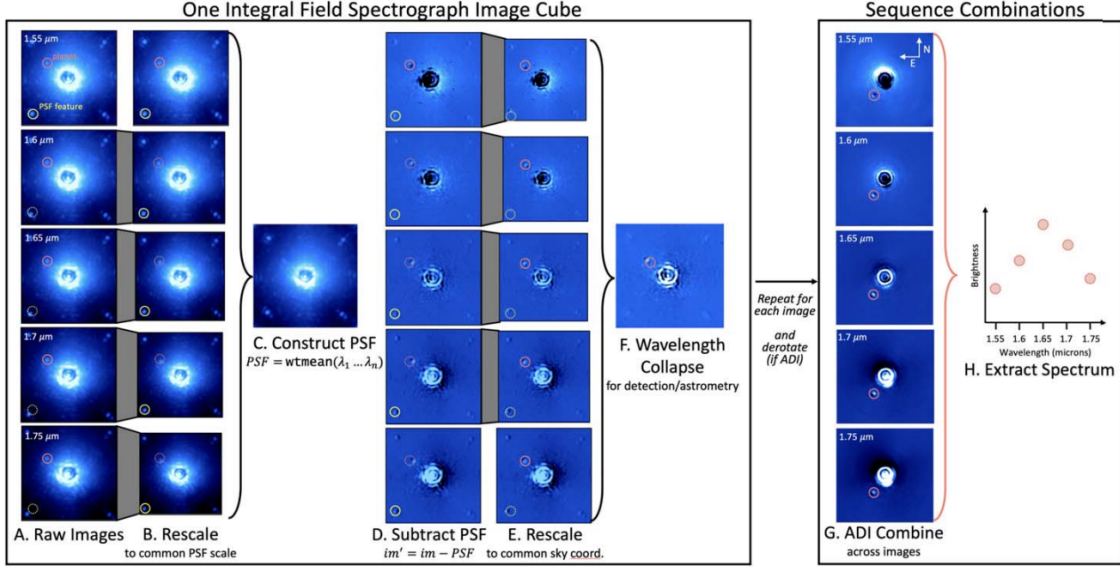


Figure 2.8: Schematic of the Spectral Differential Imaging technique (Follette, 2023).

as possible. It works by identifying the principal components of the data, which are variables that capture the most variance in the dataset (i.e. common patterns). Karhunen-Loève Image Processing (KLIP) is an application of PCA in HCI (Soumer et al., 2012). It estimates the stellar PSF and speckle noise to subtract it from the science data. Considering a HCI sequence  $(n, x, y)$  where  $n$  is the number of frames obtained during the observation, the steps to perform PCA are:

1. Subtraction of the temporal mean from each frame. After this, each subtracted frame is flattened into one-dimensional vectors and stacked into a matrix  $X \in \mathbb{R}^{N \times D}$ , where  $N$  is the number of frames and  $D$  is the number of pixels per frame.
2. Calculation of the projection matrix  $U \in \mathbb{R}^{D \times K}$ , which is the PCA basis for the low-dimensional space data. The elements of this matrix are the “principal components”, where  $K$  is the number of components chosen.
3. Projection of the data into the chosen low dimensional space, obtaining a matrix  $A \in \mathbb{R}^{N \times K}$ . This matrix contains the coefficients of the principal compo-



nents that best represent the starlight and speckles. The data is then reconstructed from the low-dimensional space as  $\hat{X} = A \cdot U^T$ , where  $\hat{X} \in \mathbb{R}^{N \times D}$ . The reconstruction  $\hat{X}$  approximates the speckle noise.

4. Subtraction of the reconstructed noise from the mean subtracted frames and stacking of the images. If the sequence is ADI or RDI, the resulting images are derotated before stacking.

This process is illustrated in Figure 2.9. In the case of ADI data, the projection matrix is calculated directly from the science data. In the case of RDI data, the principal components are calculated from the reference frames.

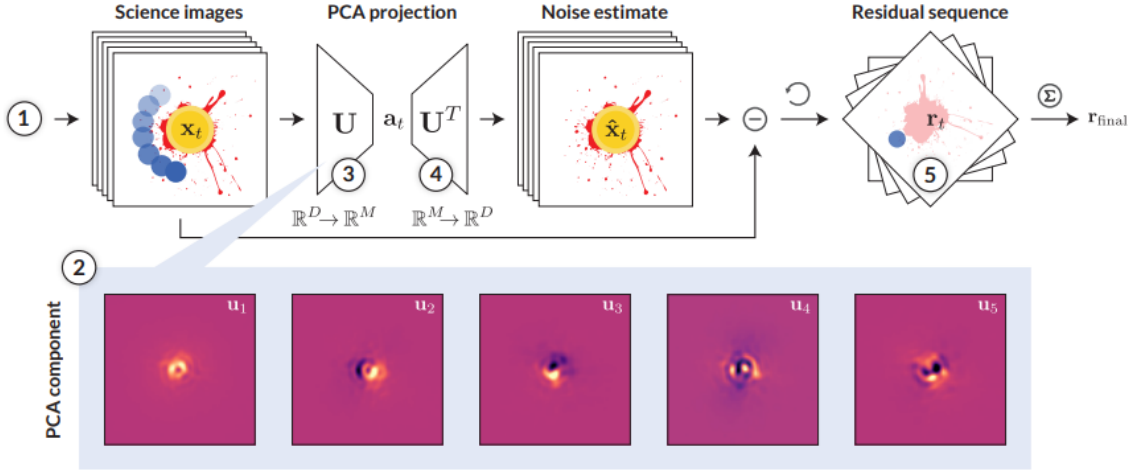


Figure 2.9: Illustration of how PCA is applied to ADI data in HCI. From [Bonse et al. \(2024\)](#).

## 2.4 The SHARK-NIR instrument

SHARK (System for coronagraphy with High order Adaptive optics from R to K band, [Farinato et al. \(2022\)](#)) is an instrument installed at the Large Binocular Telescope (LBT), which is located on Mount Graham in Arizona, United States. The

LBT comprises two identical 8.41-meter telescopes positioned side-by-side with a 22.8-meter separation. Mounted on a common altitude-azimuth structure, they provide a combined effective aperture of a single 11.8-meter telescope.

SHARK is composed of two channels: a visible arm and a near-infrared arm, each installed on opposite sides of the telescope. SHARK-VIS operates across wavelengths from  $0.5\mu\text{m}$  to  $1\mu\text{m}$ , while SHARK-NIR covers the range from  $0.96\mu\text{m}$  and  $1.7\mu\text{m}$ , providing spectral coverage from B to H bands.

SHARK-NIR began its commissioning stage in January 2023. This cutting-edge instrument is equipped with extreme adaptive optics, providing enhanced imaging and spectroscopic capabilities. During the commissioning process, calibration and optimization procedures were performed to ensure peak performance, achieving Strehl ratios greater than 98%. The subsequent science verification phase, which started in October 2023, aimed to validate the instrument's capabilities through targeted observations, such as the protoplanetary disk MWC758.

The instrument offers four distinct observing modes: classical imaging without coronagraph, coronagraphic imaging, dual-band imaging, and long-slit coronagraphic spectroscopy, providing versatile options for astronomical observations. The instrument is equipped with a sophisticated coronagraphic system, comprising three Shaped Pupil masks, a Gaussian Lyot coronagraph, and a Four-Quadrant Phase Mask, enabling the suppression of unwanted light and the enhancement of contrast for the observation of faint objects.

The instrument's specifications include a Field of View (FoV) of  $18\times 18$  arcseconds, and a detector of  $2048\times 2048$  pixels with a pixel scale of  $14.5$  mas/pixel, providing fine spatial resolution. Furthermore, the instrument's opto-mechanical design incorporates robust mechanical structures, precise optics, and advanced control systems to guarantee the instrument's efficacy. Figure 2.10 shows the optical path within the instrument while figure 2.11 shows the distribution of its key components. These components include the Atmospheric Dispersion Corrector (ADC), apodizer wheels, mirrors, Tip-Tilt Wavefront Sensor (TT WFS), and pupil plane wheel for corona-

graphic operations, among others.

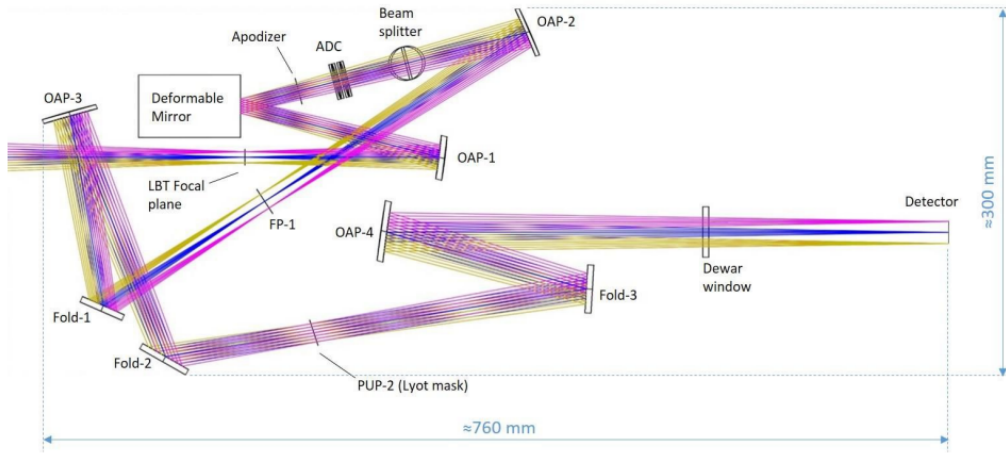


Figure 2.10: Optical path followed by the light inside the SHARK-NIR instrument (Farinato et al., 2016)

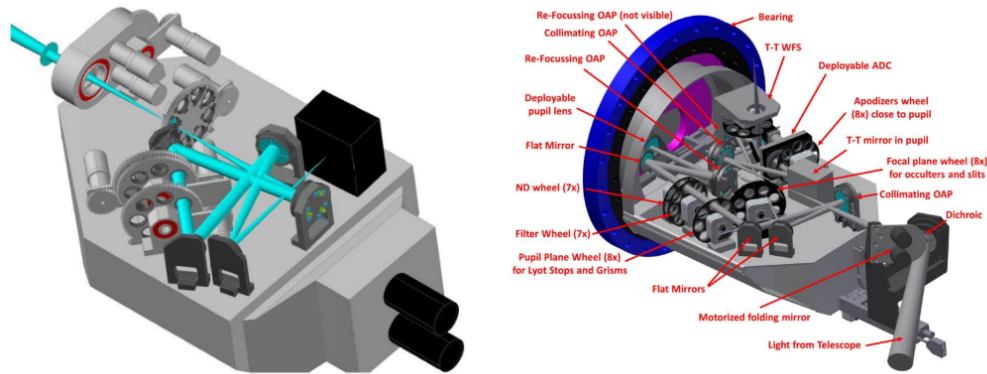


Figure 2.11: Opto-mechanical layout of the SHARK-NIR optical bench. Merged from Farinato et al. (2014) and Farinato et al. (2016)

## SHARP

The SHARP data reduction pipeline (SHARK Pipeline) is a specialized tool developed by D. Mesa to process raw data captured by the SHARK-NIR instrument. This

pipeline is adapted specifically to the specific characteristics and requirements of the SHARK-NIR data.

The purpose of this section is to provide a guide on the reduction of coronagraphic data with SHARP. For the other two observation modes (DBI and LSS), the steps are explained in the SHARK-NIR data reduction pipeline description document.

The analysis with SHARP is divided into various steps, each assigned to a different procedure in the pipeline. The configuration and workflow of SHARP are controlled by the configuration file. This file is created by SHARP before starting the data reduction steps. The configuration file consists of several sections. The first one is the ‘do it’ section, where the user decides if to do (or not) each step of the data reduction. The other sections depend on the observing mode of SHARK-NIR and each deals with a different part of the reduction, by setting the parameters that will be used for each procedure.

### Input files

Currently, SHARP only requires the raw data files captured by the instrument. The common outputs given by SHARK-NIR are:

- Files *\*CI.fits* : Scientific coronagraphic images. If they are 2D images, a third dimension must be added in order to run the pipeline. This means that the dimensions of the images must be [X, Y (detector coordinates), 1]. Usually, the images are not centered in the image coordinates.
- Files *\*GEN.fits* : Non-coronagraphic images. These files correspond to the same target observed without coronagraph, which are used for flux calibration. As for the coronagraphic images, these files must be 3D arrays.
- Files *\*DI.fits* : Background images. This includes the dark files for the coronagraphic and non-coronagraphic images, and the flat field files. The pipeline

recognizes them by the exposure time and the image type ([DARK, BACKGROUND] and [FLAT, LAMP], respectively).

### SHARP Procedures

To initiate the pipeline, users are required to ensure that all raw files are placed within a designated directory named “*raw*”. It is highly recommended that this *raw* directory is located within another folder specifically dedicated to the current observation or target, to isolate it from unrelated data and facilitate organization. This guarantees that the pipeline can access and recognize the necessary input files.

The SHARP steps for the Direct Imaging observation mode are described here.

- **doinput**: Creation of the *inputfile*, *calib* and *products* directories to store the outputs of each procedure and the input files to initialize them. It search for the image type and exposure times in the headers to differentiate the files.
- **dobck**: Creation of the master dark/background for science data reduction. It requires at least one dark/background file with the same exposure time as the science frames. The output is the master background file and a bad pixel map file.
- **dobckflux**: Creation of the master dark/background for the flux calibration data reduction. It follows a similar process to the previous step, but requires dark, background, or sky files with exposure times matching those of the flux calibration frames. The output is a master background file and a bad pixel map file for the flux calibration data.
- **doflat**: Creation of the master flat. It requires at least 5 flat files obtained with different exposure times and the bad pixel map created in the previous step. The output is a master flat file and a bad flat file.

- **doposcen**: Determination of the position of the star's center behind the coronagraph. This step is required only for coronagraphic observations. The output is a text file with the x and y coordinates for the center of the star.
- **doima**: Reduction of the scientific images using the raw scientific frames and the output of the calibration steps listed above. It also performs centering procedure. The output are the reduced images. These will be stored in the *products* folder.
- **doimaflux**: Reduction of the flux calibration images. Similar to the previous step but with different input files. The output are the reduced images for flux calibration. These will be stored in the *calib* folder.
- **doflux**: Definition of flux normalization for subsequent data reduction. Is specifically required for coronagraphic observations. This step utilizes the reduced images from the previous flux calibration step.
- **doconvert**: All reduced scientific frames are combined into a single datacube for further data reduction (e.g. speckle subtraction procedure, ADI). Normalization using the previously determined factor is performed. Additionally, provides one file containing the rotation angles needed for each frame to orientate them with North up and East left.
- **dopca**: Speckle subtraction via PCA. It results in a processed image where the speckle pattern is removed, highlighting potential point sources. Additionally, the datacube is de-rotated using the previous output.

## Output files

The output files are produced in the `doconvert` procedure. The main files are:

- File `*center_im.fits` : Master reduced cube. It corresponds to a 3D array, whose dimensions are : X, Y (detector coordinates), and number of frames (temporal dimension). The star is centered in the detector array.

- File `*rotnth.fits` : List of parallactic angles. It corresponds to an array containing the angle to rotate each frame.

These files are the essential inputs for post-processing procedures, such as ADI. This could be done using SHARP or any other script, software or library.

### Output of the PCA procedure

As mentioned in the steps of the pipeline, SHARP performs speckle subtraction through PCA and de-rotates the cube in the usual ADI way. The output of this procedure is:

- File `imgmedian_pcafin.fits` : ADI+PCA final image. It corresponds to the median of the de-rotated cube. The dimensions of this image are [X, Y (detector coordinates)].

## 2.5 The SPHERE instrument

SPHERE (Spectro-Polarimetric High-contrast Exoplanet REsearch, [Beuzit et al. \(2019\)](#)) is an instrument installed on the 8.2-meter Unit Telescope 3 (UT3) of the Very Large Telescope (VLT) at Paranal Observatory in Chile. Its primary objective is to detect and study new giant exoplanets orbiting nearby stars using direct imaging techniques.

SPHERE is designed for direct imaging and spectroscopic characterization of exoplanets. It operates in both visible and near-infrared wavelengths, providing high-contrast imaging capabilities over a small field of view around bright targets. The instrument comprises three main subsystems (Figure 2.12):

- IRDIS (InfraRed Dual-band Imager and Spectrograph, [Dohlen et al. \(2008\)](#)):

Offers a field of view of  $11'' \times 11''$  with a pixel scale of  $12.25 \text{ mas/pixel}$ . It covers a spectral range of  $0.95 - 2.32 \mu\text{m}$  in broad and narrowband filters.

- IFS (Integral Field Spectrograph, [Claudi et al. \(2008\)](#)): Covers a  $1.73'' \times 1.73''$  field of view and a wavelength range of  $0.95\text{-}1.65 \mu\text{m}$ . Its resampled pixel scale is  $7.46 \text{ mas/pixel}$ .
- ZIMPOL (Zurich Imaging Polarimeter, [Schmid et al. \(2018\)](#)): Operates in visual and infrared wavelengths, covering a spectral range of  $500 - 900 \text{ nm}$  in broad- and narrowband filters. It offers a FoV of  $3.5'' \times 3.5''$  with a pixel scale of  $7 \text{ mas/pixel}$ .

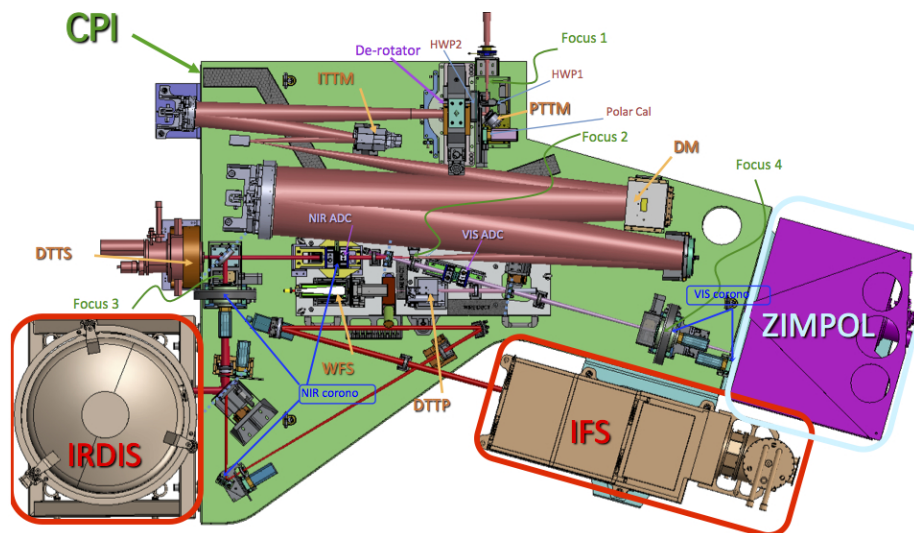


Figure 2.12: Layout of the SPHERE Common Path Infrastructure. Credits: [ESO](#)

SPHERE incorporates an extreme adaptive optics system called SAXO (SPHERE Adaptive eXtreme Optics, [Fusco et al. \(2016\)](#)), which corrects for atmospheric turbulence at  $1380 \text{ Hz}$ , achieving Strehl ratios greater than  $75\%$  in H-band. The instrument also has various coronagraphs to block the starlight (classical or apodized Lyot coronagraphs, 4QPM). SPHERE offers multiple observing modes, including dual-band imaging, long-slit spectroscopy, classical imaging, and dual-polarimetric imaging.



The data are reduced by the SPHERE High Contrast Data Center (HC-DC, [Delorme et al. \(2017\)](#)) which performs classical reduction steps including recentering, bad pixel correction, dark subtraction, flat field correction, wavelength dispersion and flux normalization of PSF and coronagraphic images. The HC-DC delivers intermediate products ready for post-processing analysis using sophisticated algorithms such as PCA in ADI, SDI and RDI.

## Chapter 3

# Exploring the morphology of the protoplanetary disk MWC 758 with SHARK-NIR

This chapter presents the first characterization of a circumstellar disk using SHARK-NIR, focusing on observations of the MWC 758 protoplanetary disk. Our study had four primary objectives: (1) searching for potential planetary companions, (2) detecting and characterizing additional disk features, (3) analyzing spiral arm motion using archival data, and (4) assessing SHARK-NIR’s detection limits in this context. Post-processing techniques were performed, such as noADI with unsharp masking, and RDI using full-frame iterative principal component analysis (IPCA) with data imputation. No detections of planetary companions within the MWC 758 system were yielded by our analysis. However, the disk’s prominent spiral arms and the eccentric cavity were successfully imaged. We compare our observations with archival data from 2015 and 2018 ([Boccaletti et al., 2021](#)), finding no discernible changes in the spiral features. This pioneering use of SHARK-NIR for disk characterization demonstrates the instrument’s capabilities and sets the stage for future high-contrast imaging studies of circumstellar environments. Section 3.2 summarizes the observa-

tions conducted and the data reduction process. The techniques employed in the post-processing are detailed in Section 3.3. The results and analysis are presented in Section 3.4.

### 3.1 The protoplanetary disk MWC 758

MWC758 (HD 36112, HIP 25793, H mag = 6.560) is an A8V Herbig star, located at RA = 05:30:28.0 and DEC = 25:19:57.0 in the Taurus stellar-forming region at a distance of  $161 \pm 2$  pc (Gaia Collaboration et al., 2023) with an estimated age of  $3.5 \pm 2.0$  Myr (Wagner et al., 2019). The protoplanetary disk of MWC 758 exhibits two prominent spiral arms, as well as other structures (Boccaletti et al., 2021), and substructures inside the spirals (Benisty et al., 2015). The disk also shows features an eccentric cavity (Dong et al., 2018). The asymmetry of the features is thought to be induced by the presence of two planetary companions, one inside and other outside the spiral arms (Dong et al., 2015). Recent observations have yielded conflicting results regarding the presence of planets in the MWC 758 system. Last year Wagner et al. (2023) confirmed the existence of MWC 758 c, orbiting the star at a projected separation of  $\sim 100$  au. The existence of a planet at this location was first theoretically predicted by Baruteau et al. (2019). Based on hydrodynamical simulations of the disk’s spiral arms, they proposed a planet with a mass of  $5 M_J$  orbiting at a separation of 140 au from the star. The subsequent observational confirmation by Wagner et al. (2023) of MWC 758 c at a projected separation of  $\sim 100$  au aligns closely with this prediction, though the observed separation is slightly smaller than the theoretical range. For the case of MWC 758 b, initially proposed by Reggiani et al. (2017), the detection is still debated. Furthermore, other recent observations have resulted in non-detections of any planets in this system (Boccaletti et al., 2021; Wagner et al., 2024).

Pages 28-37 omitted because based on unreleased collaboration data.

# Chapter 4

## Characterization of the young HD 95086 system with SPHERE

This chapter presents SPHERE observations of the HD 95086 system, exploiting the capability of SPHERE to observe using the "star-hopping" technique that allows to alternate or "hop" between the star and a reference star every 5-10 minutes to optimize the RDI strategy. With this technique were obtained promising results on another similar system (HR 8799, [Wahhaj et al. \(2021\)](#)).

Figure 4.1 illustrates the current understanding of the HD 95086 system and the motivation behind our observational approach. As shown in panel c, previous observations have hinted at the presence of a second planet candidate, HD 95086 c, located at a separation of 168 mas. Our study aims to infirm or confirm this candidate using the star-hopping technique, which is expected to improve our detection limits as illustrated in panel d.

Additional objectives of this study are to (1) conduct astrometric, photometric and spectral measurements of the known planet HD 95086 b, (2) searching for additional planets in the system, and (3) provide constraints on the location and mass of potential undetected planets. In addition to the techniques used in the analysis of MWC

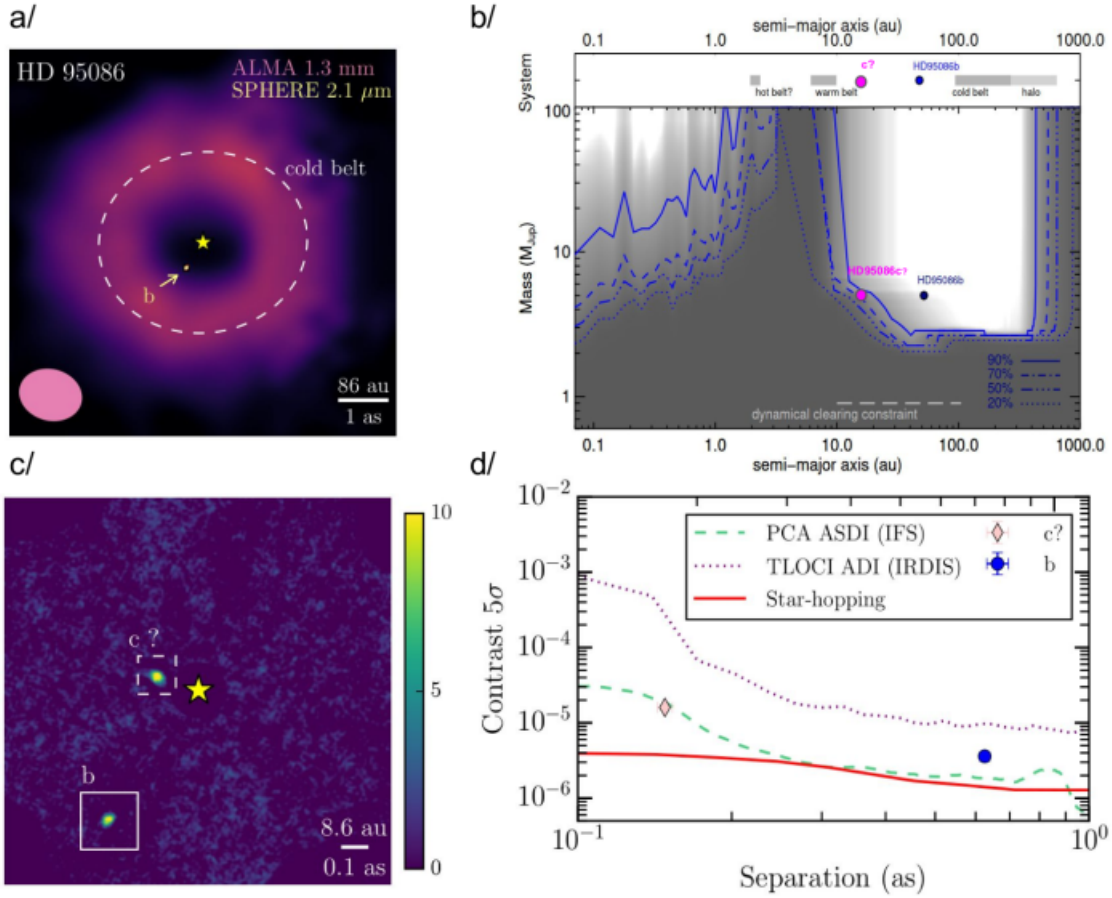


Figure 4.1: a/ Composite ALMA-continuum (at 1.3 mm) and SPHERE-IRDIS image of HD 95086 (see [Su et al. \(2017\)](#); [Chauvin et al. \(2018\)](#)). The exoplanet b is detected at K1-band (sep = 620 mas, P.A. = 148.2 deg). b/ HARPS and SPHERE combined detection limits given as a function of the planet mass and semi-major axis considering planet(s) - disk coplanar configuration. The disk architecture with the planet(s) is reported on the top. c/ SPHERE-IFS PACO-ASDI reduction of HD 95086 showing the planet b (sep = 620 mas, P.A.=148.2 deg) together with the second planet candidate c ( $\rho = 168$  mas, PA = 69.1 deg). d/ SPHERE detection limits with IFS (PCA-ASDI processing) and IRDIS (TLOCI processing) together the predicted performances of the IFS PCA-RDI star-hopping mode for HD 95086. Credits: G. Chauvin, C. Desgrange.

758 in the previous chapter, we employed multi-spectral differential imaging (mSDI) for integral field unit spectroscopy (IFS) data. We compare our observations with those made in 2018 and presented in [Desgrange et al. \(2022\)](#). Our analysis did not yield detections of new planetary companions within the HD 95086 system. However, we successfully obtained astrometry and photometry measurements of HD 95086 b and extracted its spectrum. Section 4.2 summarizes the observations conducted and the data reduction process. The techniques employed in the post-processing are detailed in Section 4.3. The forward modeling of HD 95086 b is presented in Section 4.4. Analysis of the detection limits is presented in Section 4.5.

## 4.1 The young system HD 95086

HD 95086 (HIP 53524, H mag = 6.867) is a  $1.6 \pm 0.1 M_{\odot}$  A8V star, located at RA = 10:57:03.0 and DEC = -68:40:02.4 in the Lower Centaurus Crux (LCC) subgroup of the Scorpius-Centaurus OB association at a distance of  $86.2 \pm 0.2$  pc ([Gaia Collaboration et al., 2023](#)) with an estimated age of  $13.3 \pm 1.1$  Myr ([Booth et al., 2021](#)). HD 95086 (Figure 4.2) hosts a debris disk with an inner warm belt and an outer cold belt extending from  $106 \pm 6$  AU to  $320 \pm 20$  AU ([Su et al., 2017](#)). Additionally, the system hosts an L-type exoplanet, HD 95086 b, discovered by [Rameau et al. \(2013\)](#), orbiting at a projected separation of  $\sim 52$  AU ([Chauvin et al., 2018](#)), with a mass of 4-5  $M_J$ . The architecture of HD 95086 is reminiscent of our Solar System, featuring a double belt architecture with a giant planet in the cavity between the belts. This similarity makes HD 95086 particularly interesting, as it could be viewed as a young, more massive (in terms of the host star and the giant planet) analog of our Solar System. Recent research has provided a detailed characterization of HD 95086 b ([Desgrange et al., 2022](#)), confirming its planetary nature and refining its orbital parameters, revealing the planet's extremely red color, typical of young, massive planets at the L spectral type transition. While HD 95086 b remains the only confirmed planet in the system, the complex disk structure hints at the possibility of additional, undetected planets. New observations acquired with JWST/MIRI

Pages 41-55 omitted because based on unreleased collaboration data.



# Chapter 5

## Conclusions

Our study included observations of two distinct exoplanetary systems: MWC 758 and HD 95086, utilizing advanced high-contrast imaging techniques. For MWC 758, we used observations acquired with SHARK-NIR in H-band ( $1.65 \mu\text{m}$ ) with a Gaussian Lyot coronagraph, processing the data using noADI with unsharp masking and RDI with iterative PCA. These observations successfully resolved the two-spiral-arm structure of the MWC 758 protoplanetary disk with unprecedented detail, particularly the full extent of the northern spiral arm and the edge of the eccentric cavity. However, we found inconclusive evidence of any companion candidate within SHARK-NIR's detection limits, including the previously reported MWC 758c by [Wagner et al. \(2023\)](#). For HD 95086, we used SPHERE/IRDIS in, K1 ( $2.103 \mu\text{m}$ ) and K2 ( $2.255 \mu\text{m}$ ) bands and SPHERE/IFS in YJH ( $0.97\text{--}1.66 \mu\text{m}$ ) bands, applying ADI and RADI techniques to star-hopping sequences. While we didn't detect new planetary candidates beyond the known planet b, we placed important constraints on additional companions. Our probability maps for both systems indicate limitations in detecting low-mass companions at various separations, with MWC 758 requiring masses greater than  $5 M_J$  at 100 AU, and HD 95086 ruling out  $3.5 M_J$  planets closer than 23 AU. Comparative analyzes with archival data showed no discernible morphological evolution in MWC 758's disk features over time. For HD

95086, our results are consistent with previous studies. Our comparison of ADI and RADi techniques demonstrated improved sensitivity using star-hopping RADi, particularly at close separations, highlighting its potential for future exoplanet detection efforts in challenging inner regions of planetary systems. While our observations did not confirm previously proposed planetary candidates in either system, they provide new constraints on the presence of giant planets and demonstrate the capabilities of advanced instruments like SHARK-NIR and SPHERE in high-contrast imaging of protoplanetary disks and exoplanetary systems.

Our study of MWC 758 using SHARK-NIR represents a significant milestone as it marks the first characterization of a circumstellar disk using this instrument. This achievement serves as a proof of concept, demonstrating SHARK-NIR's capabilities in high-contrast imaging of complex disk structures. This pioneering use of SHARK-NIR for disk characterization sets the stage for future detailed investigations of protoplanetary and debris disks, potentially leading to improved understanding of disk evolution and planet formation processes. In the broader context of exoplanet research, our work on both MWC 758 and HD 95086 advances our understanding of these systems and contributes to the ongoing refinement of exoplanet detection and characterization techniques. Future observations will be essential for further revealing the complexities of these and similar planetary systems.

Throughout this thesis research, I experienced significant professional growth, developing both hard and soft skills. On the technical side, I delved into high-contrast image data processing, facing and overcoming numerous image processing challenges. I learned how to apply advanced algorithms for speckle suppression and PSF subtraction. This experience sharpened my programming skills, particularly in Python and specialized astronomical software packages.

Complementing these technical abilities, I also developed essential soft skills. Collaborating with colleagues from various institutions, both remotely and in-person, improved my communication and adaptability in diverse environments. Attending an international conference provided the opportunity to present my findings and net-

work with other researchers, further boosting my confidence and presentation skills. Additionally, my participation in the exoplanet team's journal club at the Lagrange Laboratory at the Côte d'Azur Observatory also honed my skills in those aspects and in critically analyzing scientific literature. This experience not only deepened my understanding of topics directly related to my work but also exposed me to a broader range of subjects within the field. This combination of technical expertise and interpersonal skills has not only contributed to the successful completion of my thesis but has also prepared me for future challenges in my academic and professional career.

# Bibliography

- Andrews, S. M., Huang, J., Pérez, L. M., et al. 2018, , 869, L41
- Baraffe, I., Chabrier, G., Barman, T. S., Allard, F., & Hauschildt, P. H. 2003, , 402, 701
- Baruteau, C., Barraza, M., P'erez, S., et al. 2019, , 486, 304
- Benisty, M., Juhasz, A., Boccaletti, A., et al. 2015, , 578, L6
- Beuzit, J. L., Vigan, A., Mouillet, D., et al. 2019, , 631, A155
- Boccaletti, A., Pantin, E., Ménard, F., et al. 2021, , 652, L8
- Bonavita, M. 2020, Exo-DMC: Exoplanet Detection Map Calculator, Astrophysics Source Code Library, record ascl:2010.008
- Bonse, M. J., Gebhard, T. D., Dannert, F. A., et al. 2024, arXiv e-prints, arXiv:2406.01809
- Booth, M., del Burgo, C., & Hambaryan, V. V. 2021, , 500, 5552
- Boss, A. P. 1997, *Science*, 276, 1836
- Bowler, B. P. 2016, , 128, 102001
- Chauvin, G. 2018, in *Society of Photo-Optical Instrumentation Engineers (SPIE) Conference Series*, Vol. 10703, *Adaptive Optics Systems VI*, ed. L. M. Close, L. Schreiber, & D. Schmidt, 1070305

- Chauvin, G., Gratton, R., Bonnefoy, M., et al. 2018, , 617, A76
- Chen, P., Shan, H., & Zhang, P. 2016, *New Astronomy*, 44, 1
- Christiaens, V., Gonzalez, C., Farkas, R., et al. 2023, *The Journal of Open Source Software*, 8, 4774
- Claudi, R. U., Turatto, M., Gratton, R. G., et al. 2008, in *Society of Photo-Optical Instrumentation Engineers (SPIE) Conference Series*, Vol. 7014, *Ground-based and Airborne Instrumentation for Astronomy II*, ed. I. S. McLean & M. M. Casali, 70143E
- Delorme, P., Meunier, N., Albert, D., et al. 2017, in *SF2A-2017: Proceedings of the Annual meeting of the French Society of Astronomy and Astrophysics*, ed. C. Reyl e, P. Di Matteo, F. Herpin, E. Lagadec, A. Lan on, Z. Meliani, & F. Royer, Di
- Desgrange, C., Chauvin, G., Christiaens, V., et al. 2022, , 664, A139
- Dohlen, K., Langlois, M., Saisse, M., et al. 2008, in *Society of Photo-Optical Instrumentation Engineers (SPIE) Conference Series*, Vol. 7014, *Ground-based and Airborne Instrumentation for Astronomy II*, ed. I. S. McLean & M. M. Casali, 70143L
- Dong, R., yuan Liu, S., Eisner, J., et al. 2018, *The Astrophysical Journal*, 860, 124
- Dong, R., Zhu, Z., Rafikov, R. R., & Stone, J. M. 2015, , 809, L5
- Esposito, T. M., Kalas, P., Fitzgerald, M. P., et al. 2020, *The Astronomical Journal*, 160, 24
- Farinato, J., Bacciotti, F., Baffa, C., et al. 2016, in *Society of Photo-Optical Instrumentation Engineers (SPIE) Conference Series*, Vol. 9909, *Adaptive Optics Systems V*, ed. E. Marchetti, L. M. Close, & J.-P. V eran, 990931
- Farinato, J., Baruffolo, A., Bergomi, M., et al. 2022, in *Adaptive Optics Systems VIII*, ed. L. Schreiber, D. Schmidt, & E. Vernet, Vol. 12185, *International Society for Optics and Photonics (SPIE)*, 1218522

- Farinato, J., Pedichini, F., Pinna, E., et al. 2014, in Society of Photo-Optical Instrumentation Engineers (SPIE) Conference Series, Vol. 9147, Ground-based and Airborne Instrumentation for Astronomy V, ed. S. K. Ramsay, I. S. McLean, & H. Takami, 91477J
- Fedrigo, E., Donaldson, R., Soenke, C., et al. 2006, in Society of Photo-Optical Instrumentation Engineers (SPIE) Conference Series, Vol. 6272, Advances in Adaptive Optics II, ed. B. L. Ellerbroek & D. Bonaccini Calia, 627210
- Follette, K. B. 2023, Publications of the Astronomical Society of the Pacific, 135, 093001
- Fujii, Y., Angerhausen, D., Deitrick, R., et al. 2018, Astrobiology, 18
- Fusco, T., Sauvage, J. F., Mouillet, D., et al. 2016, in Society of Photo-Optical Instrumentation Engineers (SPIE) Conference Series, Vol. 9909, Adaptive Optics Systems V, ed. E. Marchetti, L. M. Close, & J.-P. Véran, 99090U
- Gaia Collaboration, Vallenari, A., Brown, A. G. A., et al. 2023, , 674, A1
- Gomez Gonzalez, C. A., Wertz, O., Absil, O., et al. 2017, , 154, 7
- Hughes, A. M., Duchêne, G., & Matthews, B. C. 2018, , 56, 541
- Mâlin, M., Boccaletti, A., Perrot, C., et al. 2024, arXiv e-prints, arXiv:2408.16843
- Marois, C., Lafrenière, D., Doyon, R., Macintosh, B., & Nadeau, D. 2006, , 641, 556
- Martinez, P., Loose, C., Carpentier, E. A., & Kasper, M. 2012, Astronomy and Astrophysics, 541
- Palma-Bifani, P., Chauvin, G., Borja, D., et al. 2024, , 683, A214
- Pavlov, A., Feldt, M., & Henning, T. 2008, in Astronomical Society of the Pacific Conference Series, Vol. 394, Astronomical Data Analysis Software and Systems XVII, ed. R. W. Argyle, P. S. Bunclark, & J. R. Lewis, 581

- Pearce, T. D. 2024, arXiv e-prints, arXiv:2403.11804
- Pfalzner, S., Dehghani, S., & Michel, A. 2022, *The Astrophysical Journal Letters*, 939, L10
- Pollack, J. B., Hubickyj, O., Bodenheimer, P., et al. 1996, , 124, 62
- Rameau, J., Chauvin, G., Lagrange, A. M., et al. 2013, , 779, L26
- Reggiani, M., Christiaens, V., Christiaens, V., et al. 2017, arXiv: Earth and Planetary Astrophysics
- Ren, B. B. 2023, , 679, A18
- Rice, K. 2022, in *Oxford Research Encyclopedia of Planetary Science*, 250
- Schmid, H. M., Bazzon, A., Roelfsema, R., et al. 2018, , 619, A9
- Sivaramakrishnan, A., Koresko, C. D., Makidon, R. B., Berkefeld, T., & Kuchner, M. J. 2001, , 552, 397
- Soummer, R., Pueyo, L., & Larkin, J. 2012, *The Astrophysical Journal Letters*, 755, L28
- Sparks, W. B. & Ford, H. C. 2002, *The Astrophysical Journal*, 578, 543
- Spiegel, D. S. & Burrows, A. 2012, , 745, 174
- Stapper, L. M. & Ginski, C. 2022, , 668, A50
- Su, K. Y. L., MacGregor, M. A., Booth, M., et al. 2017, , 154, 225
- Su, K. Y. L., Morrison, S., Malhotra, R., et al. 2015, , 799, 146
- Tokunaga, A. T. & Jedicke, R. 2007, in *Encyclopedia of the Solar System (Second Edition)*, second edition edn., ed. L.-A. McFadden, P. R. Weissman, & T. V. Johnson (San Diego: Academic Press), 719–734

- Vigan, A., Moutou, C., Langlois, M., et al. 2010, , 407, 71
- Wagner, K., Leisenring, J., Cugno, G., et al. 2024, *The Astronomical Journal*, 167, 181
- Wagner, K., Stone, J., Skemer, A., et al. 2023, *Nature Astronomy*, 7, 1208
- Wagner, K., Stone, J. M., Spalding, E., et al. 2019, *The Astrophysical Journal*, 882, 20
- Wahhaj, Z., Milli, J., Romero, C., et al. 2021, , 648, A26
- Wang, J. J., Ruffio, J.-B., De Rosa, R. J., et al. 2015, pyKLIP: PSF Subtraction for Exoplanets and Disks, *Astrophysics Source Code Library*, record ascl:1506.001
- Wyatt, M. C. 2008, , 46, 339
- Zurlo, A., Goździewski, K., Lazzoni, C., et al. 2022, , 666, A133



# Appendix A

## Observational conditions for HD 95086

SPARTA information HD95086 Star-hopping, IFS 2021

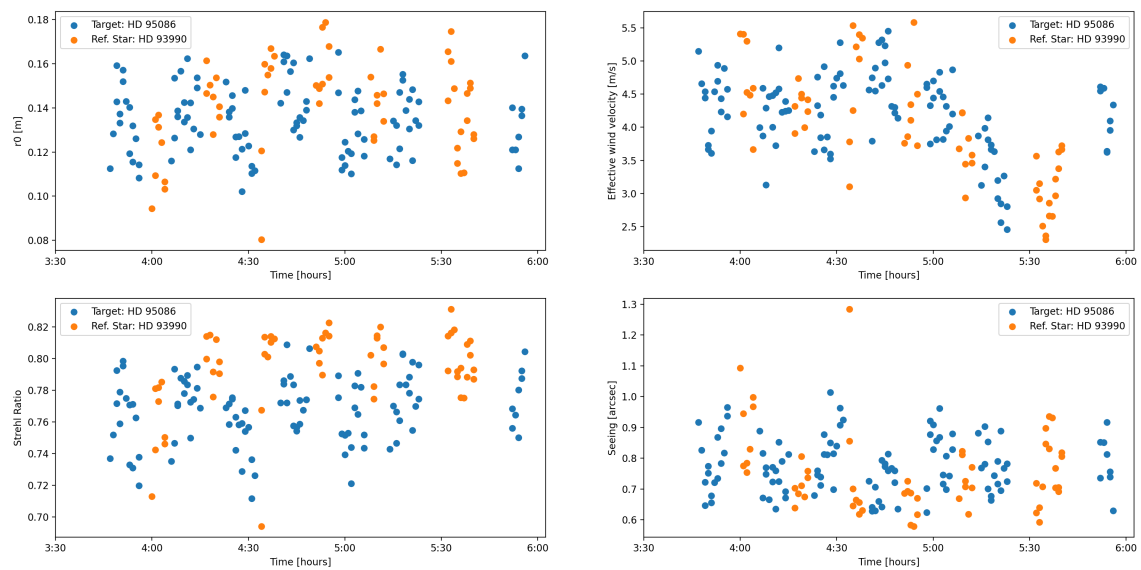


Figure A.1: Temporal evolution of the observing conditions during the observations for the 2021-03-10 epoch.

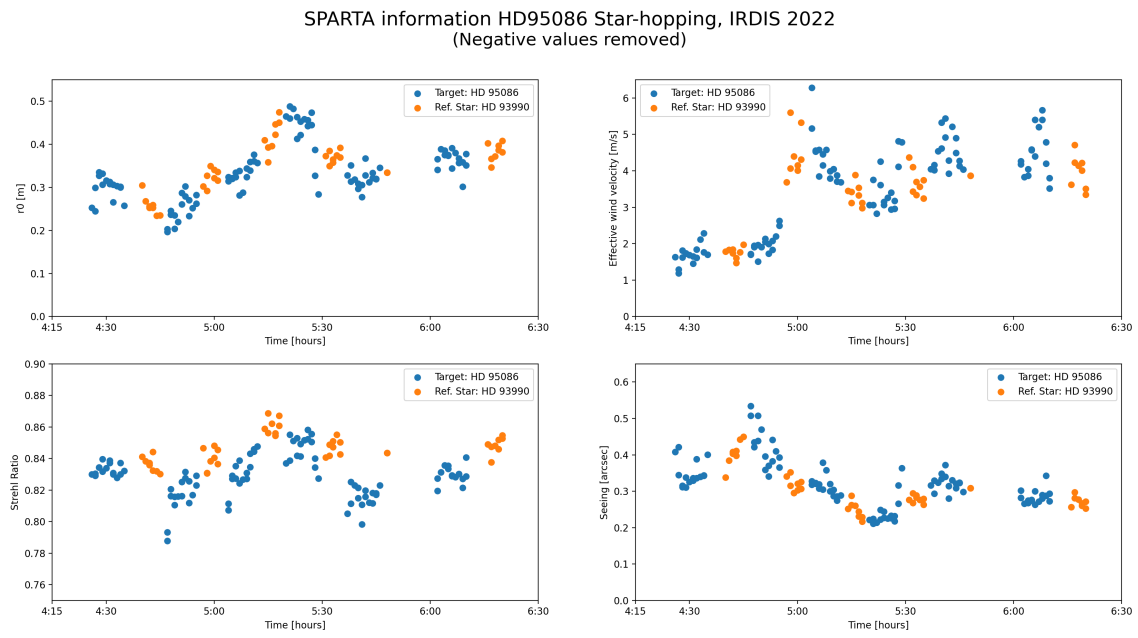


Figure A.2: Temporal evolution of the observing conditions during the observations for the 2022-03-10 epoch.

# Appendix B

## Frame Correlation Analysis for Image Filtering

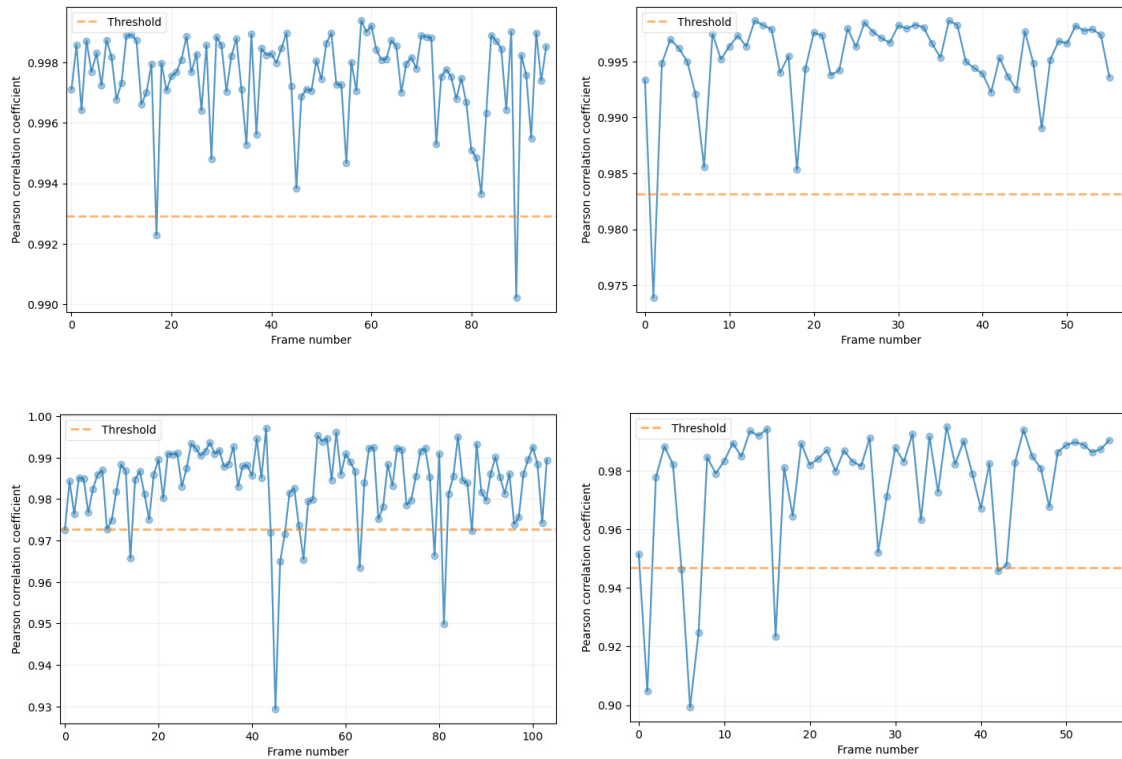


Figure B.1: Correlation of the frames in the IRDIS (top) and IFS (bottom) sequences for the 2021 epoch. *Right*: Science star. *Left*: Reference star.

APPENDIX B. FRAME CORRELATION ANALYSIS FOR IMAGE FILTERING

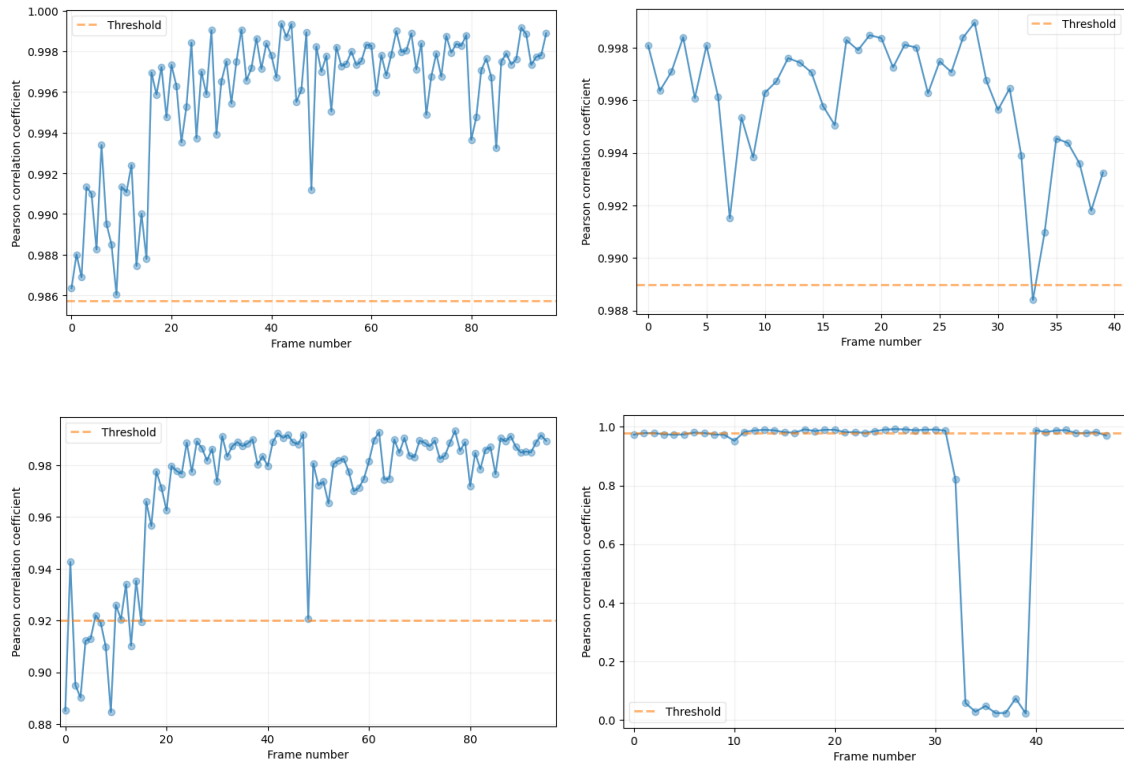



Figure B.2: Correlation of the frames in the IRDIS (top) and IFS (bottom) sequences for the 2022 epoch. *Right*: Science star. *Left*: Reference star.




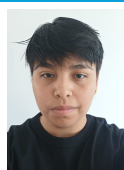
# Appendix C

## Poster Presentation: Sagan Summer Workshop



**Detection Capabilities of SHARK-NIR's High-Contrast Imager at the LBT**

Macarena Vega-Pallauta  
 Dipartimento di Fisica, Università di Roma Tor Vergata, Rome, Italy  
 Observatoire de la Côte d'Azur, Nice, France  
 contract: macarena.vega@oca.eu

---

### Summary

SHARK-NIR is a near-infrared instrument developed for the Large Binocular Telescope (LBT) under the "2014 Call for Proposals for Instrument Upgrades and New Instruments". It offers both imaging and spectroscopy, enhanced by its Extreme- $\Delta O$  system. Since its commissioning, it has performed five observation runs focusing on the newly formed stars in the Taurus constellation. Here, we describe the instrument, and provide the latest detection limits based on recent observations of HIP 11696 and MWC 758 in coronagraphic mode. Our results demonstrate impressive sensitivity down to  $10E-7$ , proving its potential in detecting faint companions in the near future.

### The Instrument

- SHARK-NIR installation at the LBT
- Operations pre on-sky

Jun - Nov 2022

Pre Commissioning phase

Jan 2023

Commissioning Phase

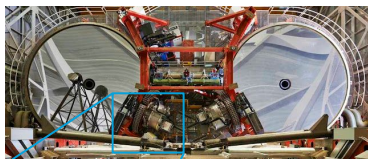
Oct 2023

Early Science Phase

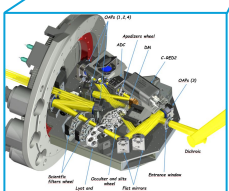
Jul 2024

Science runs

- Tests and characterization on-sky
- **First imaging sequence**
- Spectroscopic mode observations



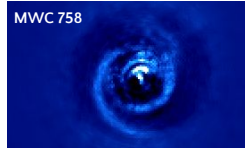
The LBT comprises two identical 8.41-meter telescopes. Combined, they provide an effective aperture of a single 11.8-meter telescope.



### Instrument Specifications

| Science Cases        | Exoplanets<br>Brown Dwarfs<br>Protoplanetary disks                            |
|----------------------|---|
| Observation Modes    | Direct Imaging<br>Coronagraphy<br>Dual-band Imaging<br>Long-Slit Spectroscopy |
| Spectral coverage    | 0.96 $\mu$ m to 1.7 $\mu$ m (Y, J, H)   |
| Detector format [px] | 2048 x 2048   |
| Waveband [ $\mu$ m]  | 0.96 - 1.7  |
| FoV ["]              | 18 x 18   |
| Pixel scale [mas/px] | 14.5  |
| Nominal Strehl       | > 98%   |

### Results

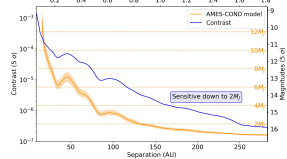


**MWC 758**

Architecture:

- MWC 758: Protoplanetary Disk
- ★ MWC 758

| Diameter (AU)     | 490              |
|-------------------|------------------|
| Spectral type     | A8Ve Herbig Star |
| Teff (K)          | 7314.0 ± 147.047 |
| Distance (pc)     | 155              |
| Age (Myr)         | 3.5 ± 2.0        |
| Mass (M $\odot$ ) | 1.5 ± 0.2        |

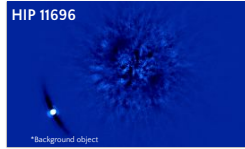


Contrast (1 $\sigma$ ) vs Separation (AU)

AMEX-COMD model (orange line)  
 Contrast (blue line)  
 Sensitive down to 2M

Observations:

- 80 min observation in Coronagraphy mode with the Gaussian Lyot and 4QPM coronagraphs.
- Atmospheric Conditions:
  - ◆ Seeing varying from 1" to 2"
- Data reduction using SHARP (SHARK Pipeline, Mesa et al. 2024, in prep)
- Post-processing: ADI, noADI, RDI using 5 modes PCA technique.

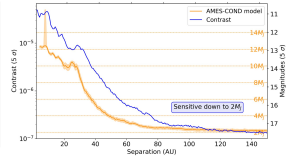


**HIP 11696**

Architecture:

- HIP 11696: High Proper Motion Star

| Spectral type     | F5V      |
|-------------------|----------|
| Teff (K)          | 5667     |
| Distance (pc)     | 49.3     |
| Age (Myr)         | 137 ± 12 |
| Mass (M $\odot$ ) | 1.326    |



Contrast (1 $\sigma$ ) vs Separation (AU)

AMEX-COMD model (orange line)  
 Contrast (blue line)  
 Sensitive down to 2M

Observations:

- 80 min observation in Coronagraphy mode with the Gaussian Lyot coronagraph.
- Data reduction using SHARP.
- Post-processing: ADI using 5 modes PCA technique.

### Coronagraphic Techniques

| Coronagraph    | IWA [mas] | OWA [mas] | Contrast     | Throughput | Band |
|----------------|-----------|-----------|--------------|------------|------|
| Gaussian Lyot  | 150       | -         | 5E-4 + 10E-6 | 56%        | J, H |
| Shaped Pupil 1 | 100       | 320       | 2E-5         | 22%        | H    |
| Shaped Pupil 2 | 140       | 320       | 10E-7        | 26%        | H    |
| 4QPM           | 40        | -         | 10E-4 + 5E-6 | 95%        | H    |

### Extreme $\Delta O$

SOUl, the Single Conjugate Adaptive Optics Upgrade for the LBT, enhances real-time atmospheric turbulence correction using pyramid wavefront sensors and deformable secondary mirrors with 672 actuators. The upgrade offers a faster loop framerate (up to 2kHz), low readout noise (0.4e-), reduced time delay (1.8ms), and 40 sub-apertures on the pupil diameter providing high spatial sampling.

### Acknowledgments

I would like to thank the SHARK-NIR consortium for providing me with the data and guidance towards this work. I acknowledge the financial assistance provided by the Sagan Exoplanet Summer Workshop and the Erasmus Mundus Joint Master (EMJM) Scholarship funded by the European Union in the framework of the Erasmus+, EMJM in Astrophysics and Space Science (MASS).







# Acknowledgements

Macarena C. Vega Pallauta acknowledges support through an Erasmus Mundus Joint Master (EMJM) scholarship funded by the European Union in the framework of the Erasmus+, Erasmus Mundus Joint Master in Astrophysics and Space Science – MASS. Views and opinions expressed are however those of the author(s) only and do not necessarily reflect those of the European Union or granting authority European Education and Culture Executive Agency (EACEA). Neither the European Union nor the granting authority can be held responsible for them.